The cellular architecture of memory modules in Drosophila supports stochastic input integration

Omar A. Hafez (ORCID:0000-0002-7846-9226)[1,5†], Benjamin Escribano (ORCID:0000-0002-1432-5952)[2†], Rouven L. Ziegler (ORCID:0000-0002-3050-7692)[2], Jan J. Hirtz (ORCID:0000-0002-4486-3057)[3], Ernst Niebur (ORCID:0000-0002-2815-9262)[1,4*] and Jan Pielage (ORCID:0000-0002-5115-5884)[2*]

[1]Zanvyl Krieger Mind/Brain Institute, Johns Hopkins University, Baltimore, MD 21218, USA.
[2]Division of Neurobiology and Zoology, Department of Biology, University of Kaiserslautern, D-67663 Kaiserslautern, Germany.
[3]Physiology of Neuronal Networks Group, Department of Biology, University of Kaiserslautern, D-67663 Kaiserslautern, Germany.
[4]Solomon Snyder Department of Neuroscience, Johns Hopkins University School of Medicine, Baltimore MD 21218, USA.
[5]Current address: Yale MD-PhD Program, Yale School of Medicine, New Haven, CT 06510, USA.

*Corresponding author(s). E-mail(s): niebur@jhu.edu; pielage@bio.uni-kl.de;
Contributing authors: ohafez1@alumni.jh.edu; benjamin.escribano@bio.uni-kl.de; roziegle@rhrk.uni-kl.de; hirtz@bio.uni-kl.de;
†These authors contributed equally to this work.

Keywords: Mushroom Body Output Neuron, Dendritic Signal Processing, Neuronal Output Tuning, Decision making, Long term memory formation

Abstract The ability to associate neutral stimuli with valence information and to store these associations as memories forms the basis for decision making. To determine the underlying computational principles, we build a realistic computational model of a central decision module within the *Drosophila* mushroom body (MB), the fly's center for learning and memory. Our model combines the electron microscopy-based architecture of one MB output neuron (MBON-α3), the synaptic connectivity of its 948 presynaptic Kenyon cells (KCs), and its *in vivo* membrane properties obtained from patch-clamp recordings. We show that this neuron is electrotonically compact and that synaptic input corresponding to simulated odor input robustly drives its spiking behavior. Therefore, sparse innervation by KCs can efficiently control and modulate MBON activity in response to learning with minimal requirements on the specificity of synaptic localization. This architecture allows efficient storage of large numbers of memories using the flexible stochastic connectivity of the circuit.

1 Introduction

Operating successfully within a complex environment requires organisms to discriminate between a vast number of potential rewarding and stressful interactions. Learning to avoid potentially harmful interactions will promote survival of individual animals and requires long-term memory mechanisms. In recent years, significant progress has been made toward our understanding of the cellular and circuit mechanisms underlying learning and memory. Despite these advances, at the computational level it remains largely unknown how the cellular and circuit architecture contributes to the efficient formation and storage of multiple memories.

Here, we use the *Drosophila melanogaster* mushroom body (MB) as a simple model system to investigate the computational principles underlying learning and memory in the context of decision making. A key advantage of the MB, the learning and memory center of the fly, is its relative simplicity in terms of the number and types of neurons compared to the mammalian brain. It has been demonstrated that the MB is required for the acquisition and recall of associative olfactory memories [1], and a wide variety of genetic tools are available to access and manipulate key cell types within the memory circuitry [2, 3]

Odor information is transmitted from the antennal lobe via projection neurons (PNs) to the Kenyon cells (KCs) of the MB. PNs are connected in a largely stochastic manner to the approximately 2000 KCs per brain hemisphere, resulting in a unique KC odor representation in individual flies [4–8]. The formation of olfactory memory within the MB circuit is assayed through experimental manipulations in which normally neutral odors are associated with either positive (reward learning) or negative (avoidance learning) valences [9].

Electrophysiological and calcium imaging studies demonstrated that any given odor activates approximately 5% of KCs [10–13]. KCs then transmit this odor information to mushroom body output neurons (MBONs) that subdivide the MB lobes into distinct structural and functional modules by virtue of their dendritic arborizations [14–17]. During associative olfactory conditioning, the behavioral response to any given odor can be altered to encode positive (approach) or negative (avoidance) behavior. The valence of the conditioned response is encoded by the activation of dopaminergic neurons (DANs) that selectively innervate the structural MB modules defined by the MBON dendrites [6].

DANs of the PPL1 cluster preferentially provide input to the vertical lobe of the MB and are activated during negative reinforcement, while DANs of the PAM cluster are activated during positive reinforcement and modulate activity in the horizontal lobe of the MB [18–23]. The majority of MBONs of the vertical lobe utilize acetylcholine as a neurotransmitter, and artificial activation of these MBONs often mediates approach behavior [15]. In contrast, the majority of MBONs of the horizontal lobe release glutamate as a neurotransmitter, and these neurons mediate avoidance behavior [15].

In vivo Calcium imaging and electrophysiological experiments demonstrated that the activity of individual MBONs can be altered by conditioning paradigms [14, 16, 24–27]. This modulation of MBON activity depends on the pairing of DAN and KC activity and results in either an enhancement or depression of the strength of the KC>MBON connection [14, 18–21]. These changes in KC>MBON connection strength occur in either the horizontal or the vertical lobe depending on the administered stimulus-reward contingencies.As a consequence, the resulting net activity of all MBONs is shifted to either approach or avoidance behavior and the behavioral response towards the conditioned stimulus during memory recall is changed [18–21]. Evidence for this MBON balance model [17] has been provided for short-term memory [15, 16, 26, 28] but to what extent, if any, such a model applies to long term memory remains unclear.

Recently, genetic tools have been created that enable genetic tagging of long-term memory engram cells in the MB [29, 30]. These studies indicate that modulation of a relatively small number of KCs is sufficient to significantly alter memory recall.

Here, we generate a realistic computational model of the core KC>MBON module that is essential for the incorporation of memories to determine the cellular basis for decision making. Prior studies [31] used "synthetic" (randomly generated) models of dendritic trees of Drosophila Projection Neurons to gain first insights into the computational processes of central neurons. Using linear cable theory, they demonstrated that voltage differences are much smaller within the dendritic trees than between the dendrites and the soma. Using a similar approach, Scheffer and coworkers [32] simulated voltage distributions in the dendritic tuft of another Drosophila neuron (EPG) but using its measured morphology, rather than random geometries. Here, we go beyond these studies by combining precise structural data including the full synaptic connectivity from the electron microscopy-based synaptic connectome [33] of the Drosophila MB with functional (electrophysiological) data of an individual MBON. This approach allows us to determine the impact of populations of KCs on MBON activity and to resolve the potential computational mechanisms underlying memory encoding. We focus on MBON-α3 (MBON-14 in the terminology of [6]) an MBON at the tip of the α lobe that is relevant for long term memory [15, 24]. We first determine the physiological parameters of MBON-α3 by patch clamp electrophysiology. We then use these parameters to generate an anatomically and physiologically realistic *in silico* model of MBON-α3 and its KC inputs. Using a variety of computational simulations, we provide evidence that MBON-α3 is electrotonically compact and perfectly suited to incorporate a substantial number of memories based on largely stochastic KC inputs.

2 Results

2.1 Electrophysiological characterization of MBON-α3

MBON-α3 is particularly suitable for computational modeling due to the availability of its complete dendritic reconstruction through electron microscopy [33]. In addition, we can access MBON-α3 genetically by using a specific Gal4 line (MB082C-Gal4) to label MBON-α3 by the expression of membrane-bound 10XUAS-IVS-mCD8::GFP (Figure 1A). In immunohistochemical co-labellings with the active zone marker Bruchpilot (Brp), we were able to visualize the dendritic input sites, the axonal projections and the cell soma of MBON-α3 (Figure 1A, arrow). We used this labelling to perform fluorescence-guided electrophysiological patch-clamp whole-cell recordings of this neuron *ex vivo* (Figure 1C,D). We carried out standard patch-clamp protocols in five cells of independent preparations and recorded all essential physiological parameters (Table 1 and Supplemental Table 1). First, we performed a continuous current-clamp protocol over $60s$ at a sampling rate of $50kHz$ which allowed us to determine the average resting membrane potential as $-56.7 \pm 2.0mV$. This value for the resting membrane potential is in line with prior measurements of MBONs *in vivo* [16]. In these recordings, we observed spontaneous firing activity of MBON-α3 with an average frequency of $12.1Hz$.

Next, we performed a current-clamp de- and hyper-polarization protocol where we recorded $400ms$ trials at a sampling rate of $50kHz$. Each trial started with $0pA$ for $10ms$, followed by a current injection of $-26pA$ to $32pA$, with $2pA$ increments for $400ms$. These protocols allowed us to evoke action potentials and to determine the resulting changes in membrane potential. An example displaying selected traces of a representative recording is shown in Figure 1F. From this data we determined the average membrane time constant as τ_m of $16.06 \pm 2.3ms$. We then performed a voltage-clamp step protocol without compensating for the series resistance. In this experiment, we recorded at $20kHz$ while applying a $5mV$ voltage step for $100ms$. This allowed us to calculate the average membrane resistance as $R_m = 926 \pm 55M\Omega$, a rather high membrane resistance when compared to similarly sized neurons [31]. MBON-α3 is thus highly excitable, with small input currents being sufficient to significantly alter its membrane potential [31, 34]. The amplitude of action potentials was rather small and similar to previously reported values for MBONs [16]. These small amplitudes are likely a result of the unipolar morphology of the neuron with a long neurite connecting the dendritic input region to the some (see below). As a resut signal propagation may partially bypass the soma [31], Figure 1F. We measured the neuron's membrane capacitance as $C_m = 16.76 \pm 1.90pF$, which classifies this cell as a mid-sized neuron [31].

To enable the calibration of the *in silico* model, we then recorded 35 trials per cell in a current-clamp injection protocol with injections of $10pA$ current pulses for $100ms$ at a sampling rate of $20kHz$. We averaged 105 traces from 3 selected example cells to a standard curve, describing the membrane kinetics of MBON-α3 in response to current injections (Figure 1G).

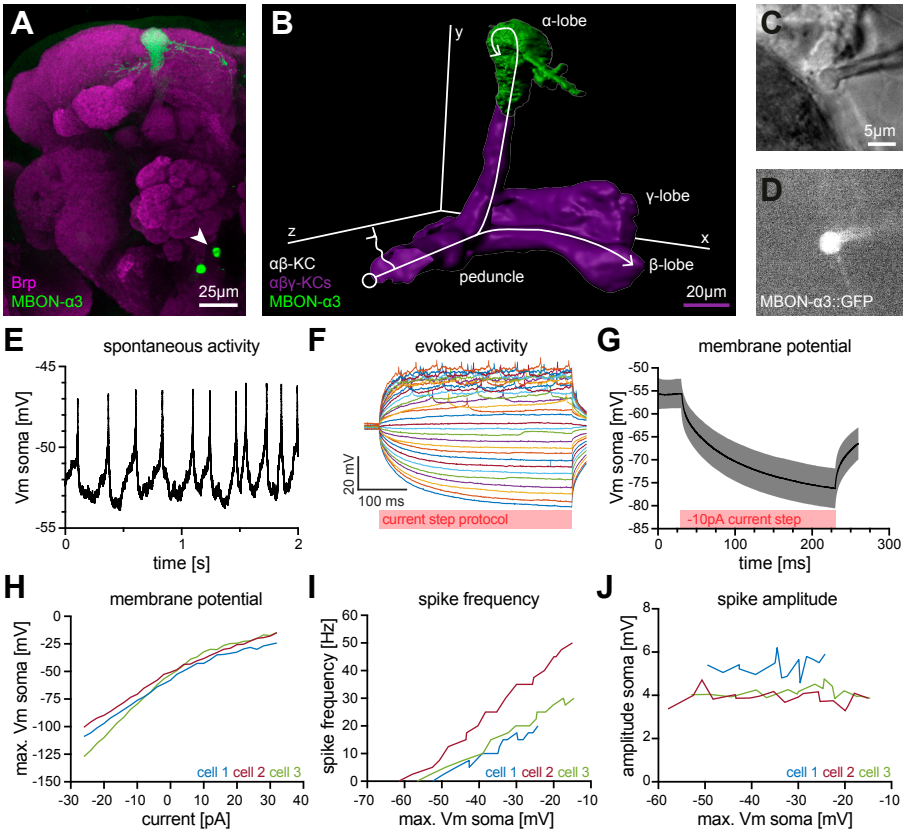

Fig. 1 Electrophysiological characterization of the MBON-α3 neuron. (A) Immunohistochemical analysis of the MBON-α3 (green, marked by GFP expression) reveals the unique morphology of the MBON with its dendritic tree at the tip of the α-lobe and the cell soma (arrowhead) at a ventro-medial position below the antennal lobes. The brain architecture is revealed by a co-staining with the synaptic active zone marker Bruchpilot (Brp, magenta). (B) Artificial superimposition of a partial rendering of MBON-α3 (green) and of $\alpha\beta\gamma$-KCs (magenta) to illustrate KC>MBON connectivity. A simplified schematic $\alpha\beta$-KC projection is illustrated in white. (C) Transmitted light image of an MBON-α3 cell body attached to a patch pipette. (D) Visualisation of the GFP-expression of MBON-α3 that was used to identify the cell via fluorescence microscopy. The patch pipette tip is attached to the soma (right side). The scale bar in C applies to C and D. (E) Recording of spontaneous activity of an MBON-α3 neuron in current clamp without current injection. (F) Recording of evoked neuronal activity of an MBON-α3 neuron with step-wise increasing injection of $400ms$ current pulses. Pulses start at $-26pA$ (bottom) with increasing $2pA$ steps and end at $+32pA$ (top). (G) Mean trace of the induced membrane polarization resulting from a $200ms$ long current injection of $-10pA$. We combined 105 trials from three different cells (35 each) to determine the membrane time constant τ_m. Gray shading indicates the SD. (H) Relative change of membrane potential after current injection. Vm is equal to the maximum depolarization of the membrane. (I) Correlation between the frequency of action potential firing and changes in membrane potential. (J) Relative change of spike amplitude after current injections. Spike amplitude represents the peak of the largest action potential minus baseline.

To to further characterize MBON-α3, we analyzed the resulting data from the current-clamp de- and hyper-polarization protocols in the three example cells (Figure 1F and Supplementary Figure S1). We recorded the absolute deflection, the action potential firing frequency, and the amplitude of action potentials for all individual cells. In all three cells, we observed that the absolute deflection of the membrane potential was proportional to the increasing current injections (Figure 1H). The action potential firing frequency increased gradually with increasing membrane potential deflections (Figure 1I), with no significant change in action potential amplitudes (Figure 1J). This is consistent with the general idea that action potentials are "all or nothing" events, and that MBON-α3 is a spike-frequency adapting neuron. These values and the tunability of the MBON-α3 are in good agreement with prior recordings of a different class of MBONs and of other central neurons in Drosophila [35]. We next used these data to generate an *in silico* model based on realistic passive membrane properties.

2.2 Constructing an *in silico* model of MBON-α3

For our *in silico* model of MBON-α3, we used the recently published electron microscopy-based connectome of the Drosophila mushroom body [33, 36]. This dataset includes the precise morphological parameters of the entire dendritic tree, the axon terminals and parts of the neurite connection to the cell soma. This dataset also includes precise location data for all 12,770 synaptic connections from the 948 innervating KCs. To build a complete morphological reconstruction of MBON-α3, we determined the length of the soma to dendrite neurite via confocal light microscopy and we incorporated this information together with all other values into the NEURON simulation environment [37] (Figure 2 (A) & (C) and Supplementary Figure S2; see Computational Model section in Materials and Methods for details). Based on the published vector data [33, 36] we subdivided the dendritic tree into 4,336 linear sections, of which 3,121 are postsynaptic to one or more of the 12,770 synaptic contacts from 948 KCs (Figure 2B). We used linear cable theory [38] to generate the *in silico* model of MBON-α3. Linear cable theory is the baseline model for neurites and the most rational approach in the absence of detailed information about potential nonlinear currents.

In previous simulations of *Drosophila* neurons, the kinetics of membrane polarisation as a response to current injections were adjusted to *in vivo* measurements through a fitting procedure [31]. We first defined the boundaries of the passive membrane parameters within NEURON's PRAXIS (principle axis) optimization algorithm and incorporated the experimentally defined passive membrane properties (Table 1). We then determined the biophysical parameters of the *in silico* neuron by current step injections of $-10pA$ for $200ms$ at the soma and by recording the neuronal voltage traces. This enabled us to fit the membrane parameters of our model neuron to the experimental data, Figure 2E. For fitting, the resulting data from the three previously selected example cells were used (Figure 2 G). The biophysical parameters that resulted

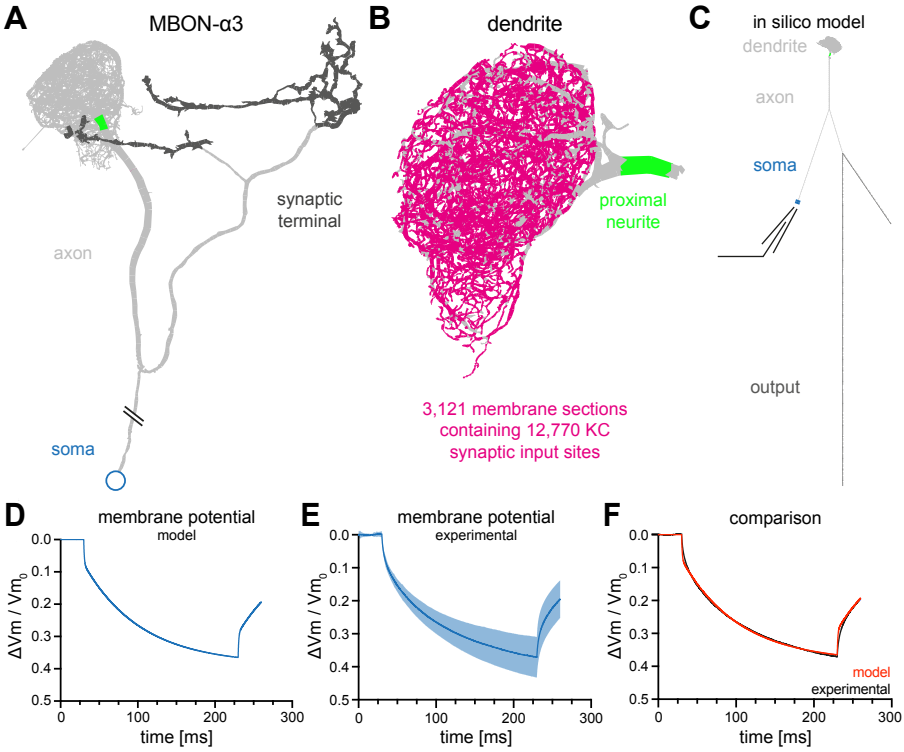

Fig. 2 Construction of a computational model of MBON-α3. (A) Electron microscopy based reconstruction of MBON-α3. Data was obtained from NeuPrint [33] and visualized with NEURON [37]. Data set MBON14 (ID 54977) was used for the dendritic architecture (A-C) and MBON14(a3)R (ID 300972942) was used to model the axon (light gray) and synaptic terminal (dark gray, A, C). The proximal neurite (bright green) was defined as the proximal axonal region next to the dendritic tree. This is the presumed site of action potential generation. Connectivity to the soma (blue) is included for illustration of the overall morphology and is not drawn to scale. (B) A magnified side view of the dendritic tree of MBON-α3. Within the dendritic tree a total of 4,336 individual membrane sections were defined (light gray area). The 3,121 membrane sections that contain one or more of the 12,770 synaptic input sites from the 948 innervating KCs are highlighted in magenta. (C) Simplified *in silico* model of MBON-α3 highlighting the size of the individual neuronal segments. We simulated recordings at the proximal neurite or at the soma. (D) Normalized trace of a simulated membrane polarization after injection of a $200ms$ long square-pulse current of $-10pA$ at the soma. (E) Normalized and averaged experimental traces (blue) with standard deviation (light blue) of our measured depolarization. (F) Comparison of a normalized induced depolarization from the model (red) and from the experimental approach (blue). The model was fitted within the NEURON environment to the measured normalized mean traces with a mean squared error between model and measured data of $0.048mV^2$. Two tailed non-parametric Spearman correlation results in r=0.9976 and p=<0.0001 between the two data sets.

from the fitting procedure are provided in the supplement. We obtained membrane kinetics that closely resembles *in vivo* current injections of $-10pA$, with a mean squared error between model and measured data of $0.0481mV^2$. For comparison, we normalized both the modelled current injection (Figure 2D)

and the traces from the *in vivo* recordings (Figure 2E) and overlayed the resulting traces in Figure 2F. These traces were highly correlated with a Spearman's correlation coefficient of $r = 0.9976$. These results indicate that we were able to generate a realistic *in silico* model of MBON-α3.

2.3 Effect of KC>MBON synaptic inputs

As KCs are cholinergic [39] we utilized previously determined parameters of cholinergic synapses to simulate synaptic input to MBON-α3. We used a reversal potential of 8.9mV and a synaptic time constant $\tau_s = 0.44ms$ as target values [40]. Individual synaptic contacts were simulated as alpha functions $(g_{max}(t - t_i) \times \exp(-(t - t_i - \tau_s)/\tau_s))$ where t_i is the time of the incoming spike and $g_{max} = 1.56 \times 10^{-11} S$, chosen to obtain response levels in agreement with the target values. The average number of synaptic contacts from a KC to this MBON is 13.47 [33], Fig. 4B. To determine the computational constraints of MBON-α3, we first stimulated each of the 3,121 dendritic sections that receive KC synaptic innervation using the described alpha-function conductance change. We then "recorded" (from our simulation) the resulting voltage excursions at the dendritic input site (Fig 3A, red), at the proximal neurite (PN, green) and at the cell soma (blue). The comparative analysis of the responses at these three locations revealed two notable features: (1) voltage excursions directly within the dendrite are faster and substantially larger than in the proximal neurite and soma, and (2), the resulting voltages in the latter two compartments are much less variable than in the dendrite and distributed within a very small voltage range (Figure 3D,E). These results indicate that the morphological architecture and biophysical parameters of MBON-α3 promote a "compactification," or "democratization," of synaptic inputs, with all inputs resulting in similar voltage excursions at the PN and soma, regardless of the strength of the initial dendritic voltage or the position on the dendritic tree.

To understand the morphological basis for the input computation, we analyzed the relation between synaptic position and local dendritic volume and the resulting voltages in the dendrite, PN and soma. Representing the distance between dendritic inputs and soma (Figure 3G) by a color code, we observed the largest voltages at distal dendritic sites with the smallest section volume (Fig. 3H,I). This architecture with the smallest dendritic sections at the most distant sites may contribute to the compactness of the dendritic tree, ensuring that even the most distant synaptic inputs result in somatic voltage deflections comparable to the most proximal ones. It is important to note again the close range of somatic responses in comparison to the large range of voltages recorded locally at the dendritic input sites (Fig. 3B). We observed a strong mean attenuation of 75.99% of the dendritic inputs at the PN and the soma which correlated with the distance from the recording site (Fig. 3F,H,I and Suppl. Fig. S3).

We next analyzed the impact of individual KCs on MBON-α3. We simulated the activation of all synapses of each individual KC that innervates

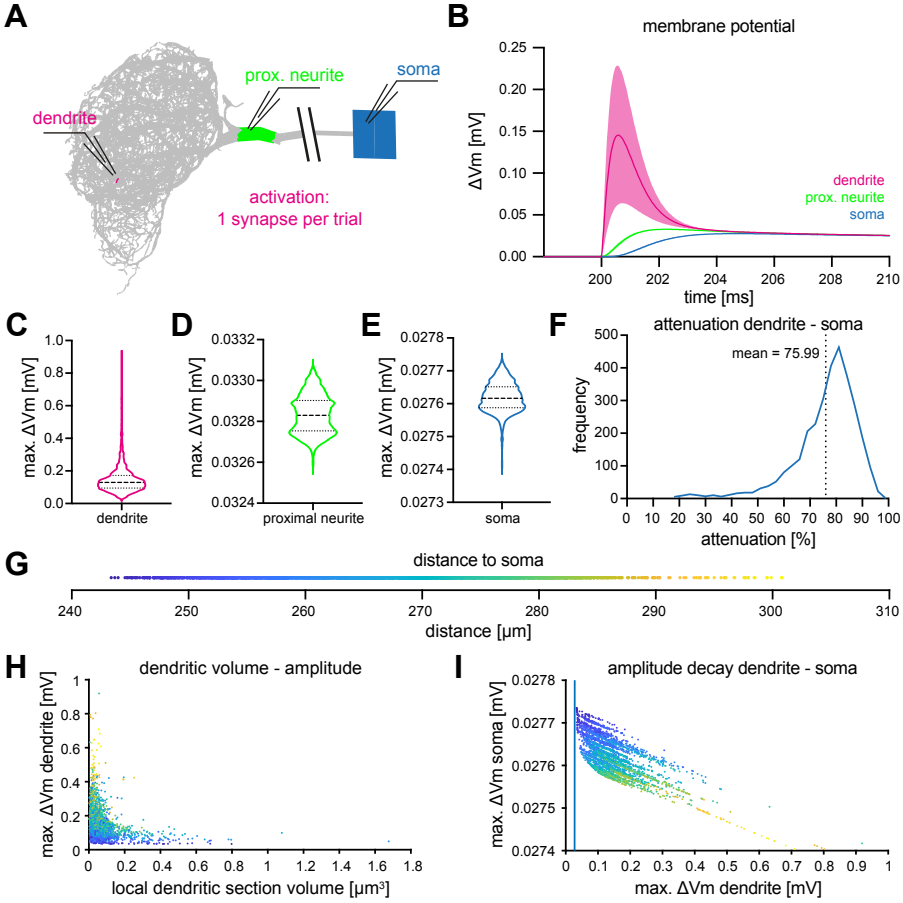

Fig. 3 Computational characterization of MBON-α3. (A) Simulated stimulation of individual synaptic input sites. Voltage deflections of synaptic currents were analyzed locally at the dendritic segment (red, next to electrode tip), the proximal neurite (green) and the soma (blue). Color code also applies to B-F. (B) Resulting mean voltages (lines) and standard deviations (shading) from synaptic activations in 3,121 individual stimulus locations (dendrite), and at the proximal neurite and soma. (C-E) Violin plots of the simulated maximal amplitudes at the dendritic section (C), the proximal neurite (D) and the soma (E) in response to synaptic activations. Dotted lines represents the quartiles and dashed lines the mean. Proportions of the violin body represent the distribution of individual data points. Note the difference in scale and compactification of the amplitudes in the proximal neurite and soma. (F) Distribution of the percentage of voltage attenuation recorded at the soma. (G) Distribution of distance between all individual dendritic sections and the soma. This color code is applied in H and I. (H) The elicited local dendritic depolarization is plotted as a function of the local dendritic section volume. (I) The soma amplitude is plotted as a function of the amplitude at individual dendritic segments. Note different scales between abscissa and ordinate; the blue line represents identity.

MBON-α3, using the synaptic parameters described above, and we recorded the simulated voltage excursions in the soma, Figure 4A. The number of synapses varied between KCs, ranging from 1 to 27 (plus one outlier with 38 synaptic contacts), with a mean of 13.47 synapses per KC (Figure 4B).

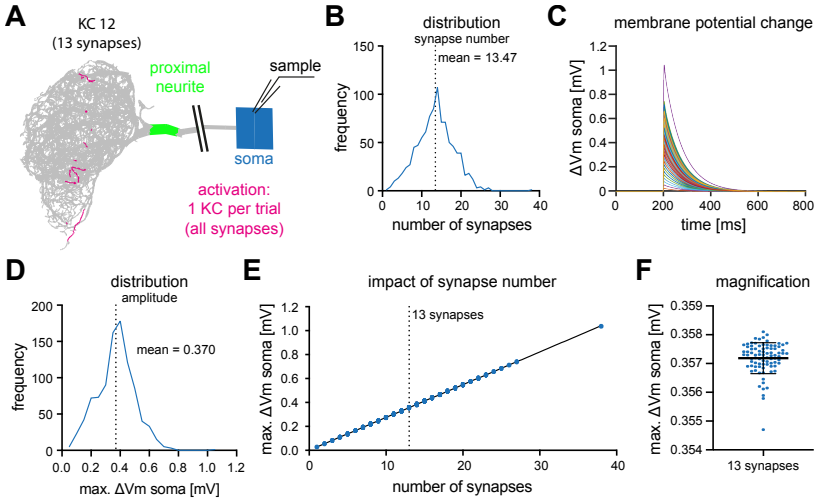

Fig. 4 MBON-α3 is electrotonically compact. (A) Simulated activation of all synapses from all 948 individual KC innervating MBON-α3. A representative example of a KC (KC12) with 13 input synapses to MBONα3 is shown. (B) Histogram of the distribution of the number of synapses per KC. (C) Membrane potential traces from simulated activation of all 948 KCs. (D) Distribution of the elicited amplitudes evoked by the individual activations of all KCs. (E) Correlation between the somatic amplitude and the number of activated synapses in the trials. (F) Distribution of the somatic amplitude evoked by the activation of all KCs with exactly 13 input synapses (each dot represents one KC).

In these simulations, we observed a wide range of voltage excursions (note the outlier in Figure 4B,C,D,E). The neuron is firmly in a small-signal operation mode, as we observed a highly linear relation between the voltage excursion and the number of synapses per KC, Fig 4E. Activating a single KC leads to a voltage excursion at the soma with a mean of 0.37mV, Fig 4D; this value is in good agreement with *in vivo* data for MBONs [16, 41]. To further analyze this linear relationship between synapse number and somatic voltage excursion, we analyzed all KCs with exactly 13 synaptic inputs to MBON-α3. This analysis revealed a highly stereotypical depolarization of the soma for all these KCs, despite wide variations in the position of the individual synaptic contacts (Figure 4E,F). These results provide further support for the compactness of MBON-α3.

2.4 Physiological and tuned activation of MBON-α3

Given that $\approx 5\%$ of the 984 KCs innervating MBON-α3 are typically activated by an odor [10, 11, 13]d, we next simulated voltage excursions in the soma

resulting from the simultaneous activation of sets of 50 randomly selected KCs. In 1,000 independent activation trials (Figure 5A), we observed highly stereotypical activation patterns, with a mean somatic depolarization of 15.24mV and only small variations in its time course (Figure 5B,C (blue)). These results are consistent with an activation of 50 KCs being sufficient to induce action potential generation in MBON-α3 (Fig 1F). The small range over which the MBON depolarization varies after input from different (random) populations of KCs, and the fact that the depolarization was strong enough to robustly fire the cell for each of the simulated odors, provides support for the current model that odor encoding in KCs is, at least to a large extent, random (stochastic) [7].

Based on *in vivo* data, two different modes of plasticity may act at the level of the KC-MBON module to alter MBON output to conditioned odors. *In vivo* imaging of short-term memory formation demonstrated alterations of KC input strength [16, 23–26, 42, 43] while recent observations of long-term memory demonstrated a specific change (increase) in the number of KCs representing the conditioned odor [44, 45].

To directly address the relative impact of these two modulations on MBON depolarization, we repeated the same simulation but now modified input strength by either altering activated KC numbers or by modulating the synaptic gain. To enable a direct comparison, we modulated each factor by 25%. First, we increased the number of activated KCs per set by 25%, from 50 to 63. This lead to a mean somatic depolarization of 18mV, a significant increase by 19% (Figure 5B,D; dark blue). Decreasing the number of activated KCs by 25%, from 50 to 38, lead to a mean somatic depolarization of 12mV, a significant decrease by 20% (Figure 5B,D; light blue). Next, we either increased or decreased synaptic strength within sets by 25%. Increase lead to a mean somatic depolarization of 18mV, a significant increase by 19% (Figure 5C,E; purple) while decrease lead to a mean somatic depolarization of 12mV, a significant decrease by 21% (Figure 5C,E; red). Averaged over all conditions, a change of input of 25% lead to a change of 20±1% in membrane depolarization. Even though the integrated synaptic conductance was changed by the same amount by our manipulation of either synaptic strength or number of activated KCs, we observed small but significant differences in the resultant mean somatic amplitudes (Figure 5F,G). Finally, we combined both manipulations by compensating an increase in KC number with a corresponding decrease in synaptic strength and vice versa. Interestingly, both manipulations resulted, on average in a significant decrease of MBON membrane depolarization (Figure 5H). Our simulations revealed a nearly linear relationship between the activated number of synapses and the measured amplitude in the soma (Figure 5I). Interestingly, we observed a difference in slope between the two different tuning modalities (Figure 5J,K,L).

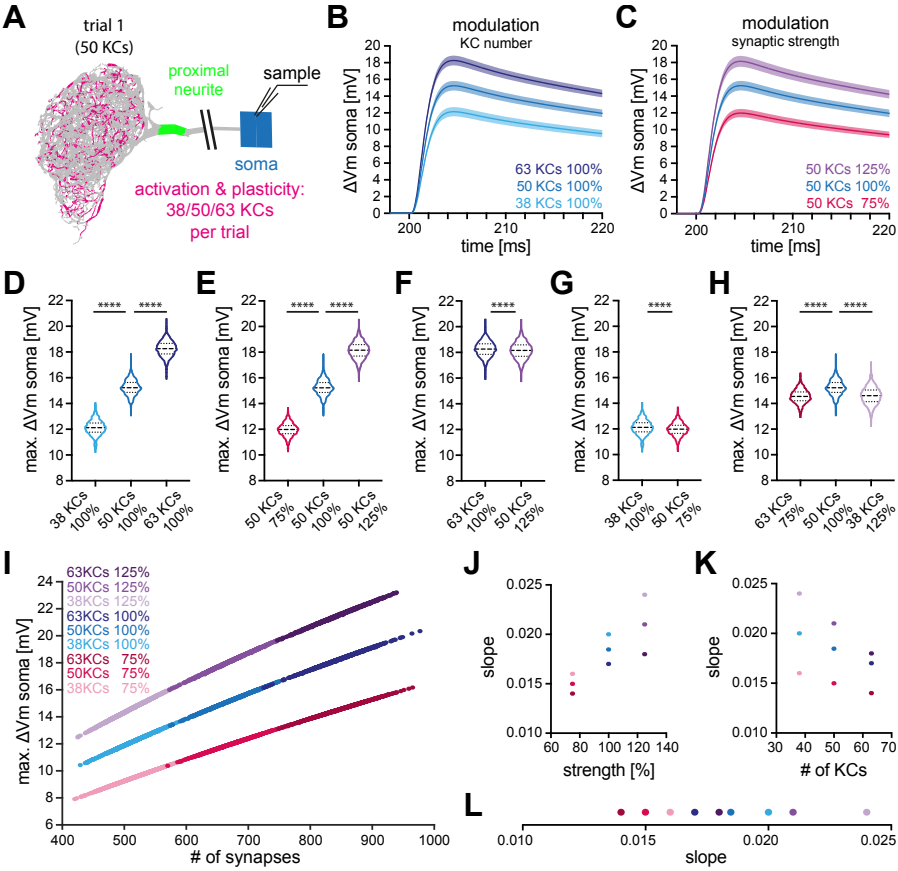

Fig. 5 Effect of KC recruitment and synaptic plasticity on MBON-α3 responses. (A) Schematic of the simulated recording paradigm. We modeled the activation of $\approx$ 5% of KCs of random combinations of identified KCs, *i.e.* we activated the anatomically correct synapse locations of 50 randomly selected KCs to mimic activation by an odor. The panel shows the distribution of activated synapses for one of these trials. We then varied the number of activated KCs by $\pm$25% around its mean of 50, *i.e.* 38, 50 and 63 KCs, and we varied synaptic strength $\pm$25% around its original value, *i.e.* 75%, 100% and 125%. (B) Mean somatic depolarizations after activating 1000 different sets of either 38 (light blue), 50 (blue), or 63 (dark blue) KCs, all at standard synaptic strength (100%). Shades represent the standard deviations. (C) Mean somatic depolarizations after activating 1000 different sets of 50 KCs at either 75% (red), 100% (blue) or 125% (purple) synaptic strength. Shades represent the standard deviations. (D, E) Violin plots of the relative amplitudes evoked by the different KC sets from (B, C). (F-G) Violin plots for the comparison of the amplitudes between the different plasticity paradigms. (F) 63 KCs at 100% *vs.* 50 KCs at 125% synaptic strength. (G) 38 KCs at 100% *vs.* 50 KCs at 75% synaptic strength. Plots in D-G use the color code from (B) and (C). (H) 63 KCs at 75% (dark red) *vs.* 50 KCs at 100% (blue) and 38 KCs at 125% (light purple) synaptic strength. See Fig. 3 for symbols in violin plots. (I) Relation between somatic depolarization and the number and strength of activated synapses. Illustrated are all tested conditions for synaptic plasticity and KC recruitment. Stimulation paradigms are color coded as shown. (J) Relation between the slope of the condition-specific linear regressions from (I) and the synaptic strength of the activated KC sets. (K) Relation between the slope of the condition-specific linear regressions from (I) and the number of recruited KCs. (L) Slopes of the condition-specific linear regressions from (I). Color codes of (J-L) as in (I). Statistical significance was tested in multiple comparisons with a parametric one-way ANOVA test (D, E and H) resulting in p=<0.0001 for all conditions, or in an unpaired parametric t-test (F and G) resulting in p=<0.0001 for all conditions. Numerical results are summarized in Supplementary Information, Table S4.

Table 1 Summary of passive membrane properties of MBON-$\alpha 3$, calculated from electrophysiological measurements from five neurons. From top to bottom: resting membrane potential (V_m) in mV, membrane time constant (τ_m) in ms, capacitance of the membrane (C_m) in pF, specific capacitance ($C_{specific}$) in μF/cm^2 and passive membrane conductance ($g_{passive}$) in S/cm^2.

Parameter	Mean ±SEM
$V_m[mV]$	-56.7 ±2.0
$\tau_m[ms]$	16.06 ±2.2
$C_m[pF]$	16.76 ±1.90
$C_{specific}[\mu\text{F}/cm^2]$	0.272 ±0.031
$g_{passive}[S/cm^2]$	$1.78 \times 10^{-5} \pm 0.11 \times 10^{-5}$

3 Discussion

The ability of an animal to adapt its behavior to a large spectrum of sensory information requires specialized neuronal circuit motifs [32]. For our understanding of the computational principles underlying learning and memory, it is essential to determine the intrinsic contributions of neuronal circuit architecture. Associative olfactory memory formation in Drosophila provides an excellent model system to investigate such circuit motifs, as a large number of different odors can be associated with either approach or rejection behavior through the formation of long-term memory within the MB circuitry. In contrast to most axon guidance processes in Drosophila that are essentially identical in all wild-type individuals, processing of odor information in the MB largely depends on the stochastic connectivity of projection neurons to KCs that relay odor information from the olfactory glomeruli to the MBONs [5, 7, 8, 46]. Individual flies display idiosyncratic, apparently random connectivity patterns that transmit information of specific odors to the output circuit of the MB. However, the role of MBONs within the circuit is largely fixed between animals and they can be mostly classified as either approach or avoidance neurons [5, 6, 15, 32, 33, 47]. Furthermore, individual KCs are not biased in their MBON connectivity but innervate both kinds of output modules, for both approach and avoidance. Learning and memory, the modulation of odor response behavior through pairing of an individual odor with either positive or negative valence, is incorporated *via* the local activity of valence-encoding DANs that can either depress or potentiate KC>MBON synaptic connections [14, 16, 18, 19, 23–25, 28, 43, 48–51]. As KC odor specificity and connectivity differ significantly between flies with respect to the number and position of KC>MBON synapses, this circuit module must be based on architectural features supporting robust formation of multiple memories regardless of specific individual KC connectivity.

Prior computational work addressing properties of central nervous system neurons in Drosophila relied on synthetic (randomly generated) data [31] or partial neuronal reconstructions [32]. We go beyond these previous studies by combining precise structural data from the electron-microscopy based synaptic connectome [33] with functional (electrophysiological) data. The structural data consists of the precise neuroanatomical structure of MBON-$\alpha 3$, including the 12,770 synaptic inputs of all its 948 innervating KCs. The neuron's functional properties were determined from *ex vivo* patch clamp recordings. Near-perfect agreement between experimentally observed and simulated voltage distributions in the dendritic tree shows that linear cable theory is an excellent model for information integration in this system. Together, we obtain a realistic *in silico* model of a central computational module of memory-modulated animal behavior, *i.e.* a mushroom body output neuron.

Our data show that the dendritic tree of the MBON is electrotonically compact, agreeing with a prior electrophysiological characterization of an MBON in locust [52]. The location of an individual synaptic input within the dendritic tree has therefore only a minor effect on the amplitude of the neuron's output, despite large variations of local dendritic potentials. This effect was particularly striking when we restricted the analysis to a population of KCs with identical numbers of synapses that all elicited highly stereotypical responses. The compactification of the neuron is likely related to the architectural structure of its dendritic tree. Together with the relatively small size of many central neurons in *Drosophila*, this indicates that in contrast to large vertebrate neurons, local active amplification or other compensatory mechanisms [53–56] may not be necessary to support input normalization in the dendritic tree. In contrast, for axons it has been recently reported that voltage-gated Na^+ channels are localized in putative spike initiation zones in a subset of central neurons of *Drosophila* [57]. Once *in vivo* electrophysiological data quantitatively describing local active currents become available, they can be incorporated into our model to further increase the agreement between model and biological system.

Encoding of odor information and incorporation of memory traces is not performed by individual KCs but by ensembles of KCs. Calcium imaging *in vivo* demonstrated that individual odors evoke activity in approximately 3-9% of KCs [10, 11]. Our simulations of 1,000 independent trials with random sets of 50 KCs, each representing one distinct odor that activates approximately 5% of the KCs innervating the target MBON, demonstrate that such activation patterns robustly elicit MBON activity to a level that matched our *in vivo* observations of odor-induced activity, as well as that found in previous studies [13, 16, 46]. The low variability of depolarizations observed in these simulations indicates that information coding by such activation patterns is highly robust. As a consequence, labeled line representations of odor identity are likely not necessary at the level of KCs since relaying information *via* **any** set of ≈50 KCs is of approximately equal efficiency. Such a model is supported by a recent computational study demonstrating that variability in parameters

controlling neuronal excitability of individual KCs negatively affects associative memory performance. The authors provide evidence that compensatory variation mechanisms exist that ensure similar activity levels between all odor encoding KC sets to maintain efficient memory performance [58].

Optical recordings of *in vivo* activity of MBONs revealed selective reductions in MBON activity in response to aversive odor training [23, 25, 26, 42, 43] or to optogenetic activation of selective DANs [16]. More generally, both depression and potentiation of MBON activity have been previously observed in different MBON modules *in vivo* [16, 23–26, 42, 43]. In addition, recent studies have observed changes in KC stimulus representations after conditioning [44, 45] that may be due to learning-dependent modulations of synaptic PN input to KCs [59]. Our computational model allowed us to implement and compare these two mechanisms changing MBON output: One is a change in the strength of the KC>MBON synapses (over a range of ±25%); the other is a change in the number of activated KCs (over the same range). Interestingly, we found almost linear relationships between the number of active KCs and the resulting depolarizations, and the same between the strength of synapses and MBON depolarization. Decreasing either of these variables by 25% significantly decreased the level of MBON activation.

Our simulation data thus shows that the KC>MBON architecture represents a biophysical module that is well-suited to simultaneously process changes based on either synaptic and or network modulation. Together with the electrotonic nature of the MBONs the interplay between KCs and MBONs thus ensures reliable information processing and memory storage despite the stochastic connectivity of the memory circuitry. While our study focuses on the detailed activity patterns within a single neuron, the availability of large parts of the fly connectome at the synaptic level, in combination with realistic models for synaptic dynamics, should make it possible to extend this work to circuit models to gain a network understanding of the computational basis of decision making.

4 Materials and Methods

Fly Stocks

Flies were reared on standard fly food at 25°C and 65% humidity. Following stocks were used in this study: 10XUAS-IVS-mCD8::GFP [60] (BDSC 32186), MB082C-Gal4 [15] (BDSC 68286).

Immunohistochemistry

Male flies expressing GFP in MBON-α3 were fixed for 3.5h at 4°C in 4% PFA containing PBST (0.2% Triton-X100). Flies were then washed for at least 3 x 30 min at RT in PBST before dissection. Dissected brains were then labelled with primary antibodies (rabbit anti-GFP (A6455, Life technologies, Carlsbad, USA 1:2000) and mouse anti-Brp nc82, Developmental Studies Hybridoma Bank, Iowa, USA, 1:200) for two nights at 4°C. After incubation, brains were washed at least 6 x 30 min in PBST. Secondary antibodies (Alexa488 (goatαrabbit) and Alexa568 (goatαmouse) coupled antibodies, Life technologies, Carlsbad, USA, 1:1000) were applied for two nights at 4°C. After a repeated washing period, brains were submerged in Vectashield (Vector Laboratories, Burlingame, USA), mounted onto microscope slides, and stored at 4°C.

Images were acquired using a confocal scanning microscope (LSM 710, Carl Zeiss GmbH, Jena, Germany) and a 25x (Plan-NEOFLUAR, NA 0.8 Korr DIC, Carl Zeiss GmbH, Jena, Germany) oil objective. Raw images were projected with Fiji [61] and cropped in Photoshop (Adobe, San José, USA). Uniform adjustments of brightness and contrast were performed.

Electrophysiology

Flies were flipped 1d after hatching to obtain 3-5d old flies. Due to the inconvenient location of the MBON-α3 soma we performed *ex vivo* recordings of the brain. For preparation, flies expressing GFP in MBON-α3 were briefly anesthetized on ice before removing the entire brain from the head. The preparation was performed in oxygenated (95% O_2 and 5% CO_2) high glucose ($260mM$) extracellular saline. As described previously, the brain was incubated for $30s$ in $0.5mg/ml$ protease (from Streptomyces griseus, CAS# 90036-06-0, Sigma-Aldrich, St. Louis, USA) containing extracellular saline [62]. The brain was then transferred to standard extracellular saline [62] (in mM: 103 $NaCl$, 3 KCl, 5 TES, 10 trehalose, 260 glucose, 7 sucrose, 26 $NaHCO_3$, 1 NaH_2PO_4, 1.5 $CaCl_2$, 4 $MgCl_2$, pH 7.3, $280-290mOsmol/kg$ adjusted with sucrose). For physiological recordings, the brain was transferred to a glass bottom chamber with continuously perfused ($2ml/min$) oxygenated standard extracellular saline and held in place by a custom made platinum frame. All patch clamp recordings were performed at room temperature similar to prior descriptions [16, 41]. A detailed description of all electrophysiological protocols is provided in Supplemental Methods.

Computational Model

Morphological data for the dendritic arborization of Drosophila MBON-α3-A as well as the locations of all its 12,778 afferent KC synapses were obtained through electron microscopy [33] (Fig. 2A'). The relative geometry of soma and axon, not contained in this published data set, was determined from a separate MBON (Fig. 2A, see Supplementary Methods). Soma and axon were approximated as five separate sections (Fig. S3), and appended to the MBON-α3-A proximal neurite. We determined the dimensions of the MBON-α3-A soma by light microscopy (Fig. 1A).

Electrophysiological properties of the neuron were determined by fitting the model response to measured data, Table S2. Somatic voltage excursions in response to current injections were recorded *in vivo* (Fig. 1G) and compared with the simulated membrane potential (Fig. 2D). By minimizing their difference we fit the simulation parameters, *viz* cytoplasm resistivity and specific membrane capacitance and conductance. Based on our recorded data. resting membrane potential was set at -55.64mV.

Cholinergic KC to MBON synapses were modeled as localized conductance changes described by alpha functions (Table S2), with a rise time of 0.44ms and a reversal potential of 8.9mV [40]. The maximal conductance for the synapses was set at $1.56 * 10^{-5} \mu S$, the value determined to achieve the target MBON depolarization from monosynaptic KC innervation [41].

All simulations were performed using the NEURON simulation environment [37]. The morphology data divided the MBON-α3-A into 4342 cylindrical sections with passive leak channels (Supplementary Table S1), with each KC synapse mapped to its nearest section of the MBON dendrite. See Supplementary Information for more details describing the model.

Statistical Analysis

Statistical analysis and visualization of data was performed in Prism 9 (GraphPad, San Diego, USA) and Matlab (MathWorks, Natick, USA). Before a statistical comparison was performed, individual groups were tested in Prism for normality and lognormality with an Anderson-Darling test. Statistical significance was tested with an unpaired parametric t-test or in case of multiple comparisons, with an ordinary corrected parametric one-way ANOVA test. Further information is provided in figure legends and in the Supplement.

Supplementary information. Extended data and methods are provided in the Supplement.

Acknowledgments. We would like to thank Glenn Turner and Toshihide Hige for insightful comments on the patch clamp analysis.

Declarations

Funding

This work was supported by NIH R01DC020123, NSF 1835202, NIH R01DA040990, NIH R01EY027544, NIH Medical Scientist Training Program Training Grant T32GM136651, and a BMBF grant.

Competing interests

The authors declare no competing interests.

Ethics approval

Not applicable

Consent to participate

Not applicable

Consent for publication

Not applicable

Availability of data and materials

All modeling data will be shared upon request. Stocks obtained from the Bloomington Drosophila Stock Center (NIH P40OD018537) were used in this study.

Code availability

All code is available upon request.

Authors' contributions

O.A.H., B.E, E.N. and J.P. designed research; O.A.H., B.E. and R.L.Z. performed research; O.A.H., B.E., R.L.Z., J.J.H., E.N., J.P. analyzed data; O.A.H., B.E., E.N. and J.P. wrote the paper

References

[1] de Belle, J., Heisenberg, M.: Associative odor learning in Drosophila abolished by chemical ablation of mushroom bodies. Science **263**(5147), 692–695 (1994). https://doi.org/10.1126/science.8303280. Accessed 2021-02-12

[2] Owald, D., Lin, S., Waddell, S.: Light, heat, action: neural control of fruit fly behaviour. Philosophical Transactions of the Royal Society B: Biological Sciences **370**(1677), 20140211 (2015)

[3] Lai, S.-L., Lee, T.: Genetic mosaic with dual binary transcriptional systems in Drosophila. Nature Neuroscience **9**(5), 703–709 (2006)

[4] Lin, H.-H., Lai, J.S.-Y., Chin, A.-L., Chen, Y.-C., Chiang, A.-S.: A Map of Olfactory Representation in the Drosophila Mushroom Body. Cell **128**(6), 1205–1217 (2007)

[5] Litwin-Kumar, A., Harris, K.D., Axel, R., Sompolinsky, H., Abbott, L.F.: Optimal Degrees of Synaptic Connectivity. Neuron **93**(5), 1153–11647 (2017). https://doi.org/10.1016/j.neuron.2017.01.030. Accessed 2019-11-22

[6] Aso, Y., Hattori, D., Yu, Y., Johnston, R.M., Iyer, N.A., Ngo, T.-T., Dionne, H., Abbott, L., Axel, R., Tanimoto, H., Rubin, G.M.: The neuronal architecture of the mushroom body provides a logic for associative learning. eLife **3**, 04577 (2014). https://doi.org/10.7554/eLife.04577. Accessed 2020-03-03

[7] Caron, S.J.C., Ruta, V., Abbott, L.F., Axel, R.: Random convergence of olfactory inputs in the Drosophila mushroom body. Nature **497**(7447), 113–117 (2013). https://doi.org/10.1038/nature12063. Accessed 2021-01-27

[8] Gruntman, E., Turner, G.C.: Integration of the olfactory code across dendritic claws of single mushroom body neurons. Nature Neuroscience **16**(12), 1821–1829 (2013). https://doi.org/10.1038/nn.3547. Accessed 2019-11-22

[9] Livingstone, M.S., Sziber, P.P., Quinn, W.G.: Loss of calcium/calmodulin responsiveness in adenylate cyclase of rutabaga, a Drosophila learning mutant. Cell **37**(1), 205–215 (1984). https://doi.org/10.1016/0092-8674(84)90316-7. Accessed 2019-11-22

[10] Campbell, R.A.A., Honegger, K.S., Qin, H., Li, W., Demir, E., Turner, G.C.: Imaging a population code for odor identity in the Drosophila mushroom body. The Journal of Neuroscience: The Official Journal of the Society for Neuroscience **33**(25), 10568–10581 (2013). https://doi.org/10.1523/JNEUROSCI.0682-12.2013

[11] Honegger, K.S., Campbell, R.A.A., Turner, G.C.: Cellular-Resolution Population Imaging Reveals Robust Sparse Coding in the Drosophila Mushroom Body. Journal of Neuroscience **31**(33), 11772–11785 (2011). https://doi.org/10.1523/JNEUROSCI.1099-11.2011. Accessed 2019-11-22

[12] Turner, G.C., Bazhenov, M., Laurent, G.: Olfactory Representations by Drosophila Mushroom Body Neurons. Journal of Neurophysiology

99(2), 734–746 (2008). https://doi.org/10.1152/jn.01283.2007. Accessed 2021-05-19

[13] Siegenthaler, D., Escribano, B., Bräuler, V., Pielage, J.: Selective suppression and recall of long-term memories in Drosophila. PLoS biology **17**(8), 3000400 (2019). https://doi.org/10.1371/journal.pbio.3000400

[14] Owald, D., Felsenberg, J., Talbot, C.B., Das, G., Perisse, E., Huetteroth, W., Waddell, S.: Activity of Defined Mushroom Body Output Neurons Underlies Learned Olfactory Behavior in Drosophila. Neuron **86**(2), 417–427 (2015). https://doi.org/10.1016/j.neuron.2015.03.025. Accessed 2019-11-22

[15] Aso, Y., Sitaraman, D., Ichinose, T., Kaun, K.R., Vogt, K., Belliart-Guérin, G., Plaçais, P.-Y., Robie, A.A., Yamagata, N., Schnaitmann, C., Rowell, W.J., Johnston, R.M., Ngo, T.-T.B., Chen, N., Korff, W., Nitabach, M.N., Heberlein, U., Preat, T., Branson, K.M., Tanimoto, H., Rubin, G.M.: Mushroom body output neurons encode valence and guide memory-based action selection in Drosophila. eLife **3**, 04580 (2014). https://doi.org/10.7554/eLife.04580. Accessed 2021-01-27

[16] Hige, T., Aso, Y., Modi, M.N., Rubin, G.M., Turner, G.C.: Heterosynaptic Plasticity Underlies Aversive Olfactory Learning in Drosophila. Neuron **88**(5), 985–998 (2015). https://doi.org/10.1016/j.neuron.2015.11.003. Accessed 2020-03-03

[17] Cognigni, P., Felsenberg, J., Waddell, S.: Do the right thing: neural network mechanisms of memory formation, expression and update in Drosophila. Current opinion in neurobiology **49**, 51–58 (2018)

[18] Handler, A., Graham, T.G.W., Cohn, R., Morantte, I., Siliciano, A.F., Zeng, J., Li, Y., Ruta, V.: Distinct Dopamine Receptor Pathways Underlie the Temporal Sensitivity of Associative Learning. Cell **178**(1), 60–7519 (2019). https://doi.org/10.1016/j.cell.2019.05.040. Accessed 2019-11-22

[19] Aso, Y., Rubin, G.M.: Dopaminergic neurons write and update memories with cell-type-specific rules. eLife **5**, 16135 (2016). https://doi.org/10.7554/eLife.16135. Accessed 2019-11-22

[20] Cohn, R., Morantte, I., Ruta, V.: Coordinated and Compartmentalized Neuromodulation Shapes Sensory Processing in Drosophila. Cell **163**(7), 1742–1755 (2015)

[21] Burke, C.J., Huetteroth, W., Owald, D., Perisse, E., Krashes, M.J., Das, G., Gohl, D., Silies, M., Certel, S., Waddell, S.: Layered reward signalling through octopamine and dopamine in Drosophila. Nature **492**(7429), 433–437 (2012)

[22] Tomchik, S.M., Davis, R.L.: Dynamics of Learning-Related cAMP Signaling and Stimulus Integration in the Drosophila Olfactory Pathway. Neuron **64**(4), 510–521 (2009). https://doi.org/10.1016/j.neuron.2009.09.029. Accessed 2019-11-22

[23] Séjourné, J., Plaçais, P.-Y., Aso, Y., Siwanowicz, I., Trannoy, S., Thoma, V., Tedjakumala, S.R., Rubin, G.M., Tchénio, P., Ito, K., Isabel, G., Tanimoto, H., Preat, T.: Mushroom body efferent neurons responsible for aversive olfactory memory retrieval in Drosophila. Nature Neuroscience **14**(7), 903–910 (2011). https://doi.org/10.1038/nn.2846. Accessed 2019-11-22

[24] Plaçais, P.-Y., Trannoy, S., Friedrich, A.B., Tanimoto, H., Preat, T.: Two Pairs of Mushroom Body Efferent Neurons Are Required for Appetitive Long-Term Memory Retrieval in Drosophila. Cell Reports **5**(3), 769–780 (2013). https://doi.org/10.1016/j.celrep.2013.09.032. Accessed 2021-02-12

[25] Jacob, P.F., Waddell, S.: Spaced Training Forms Complementary Long-Term Memories of Opposite Valence in Drosophila. Neuron **106**(6), 977–9914 (2020). https://doi.org/10.1016/j.neuron.2020.03.013. Accessed 2021-09-06

[26] Perisse, E., Owald, D., Barnstedt, O., Talbot, C.B., Huetteroth, W., Waddell, S.: Aversive Learning and Appetitive Motivation Toggle Feed-Forward Inhibition in the Drosophila Mushroom Body. Neuron **90**(5), 1086–1099 (2016). https://doi.org/10.1016/j.neuron.2016.04.034. Accessed 2019-11-22

[27] Felsenberg, J., Jacob, P.F., Walker, T., Barnstedt, O., Edmondson-Stait, A.J., Pleijzier, M.W., Otto, N., Schlegel, P., Sharifi, N., Perisse, E., Smith, C.S., Lauritzen, J.S., Costa, M., Jefferis, G.S.X.E., Bock, D.D., Waddell, S.: Integration of Parallel Opposing Memories Underlies Memory Extinction. Cell **175**(3), 709–72215 (2018). https://doi.org/10.1016/j.cell.2018.08.021. Accessed 2019-11-22

[28] Cohn, R., Morantte, I., Ruta, V.: Coordinated and Compartmentalized Neuromodulation Shapes Sensory Processing in Drosophila. Cell **163**(7), 1742–1755 (2015). https://doi.org/10.1016/j.cell.2015.11.019. Accessed 2020-12-14

[29] Siegenthaler, D., Escribano, B., Bräuler, V., Pielage, J.: Selective suppression and recall of long-term memories in Drosophila. PLoS Biology **17**(8), 3000400 (2019)

[30] Miyashita, T., Kikuchi, E., Horiuchi, J., Saitoe, M.: Long-Term Memory Engram Cells Are Established by c-Fos/CREB Transcriptional Cycling.

Cell Reports **25**(10), 2716–27283 (2018). https://doi.org/10.1016/j.celrep.2018.11.022

[31] Gouwens, N.W., Wilson, R.I.: Signal Propagation in Drosophila Central Neurons. Journal of Neuroscience **29**(19), 6239–6249 (2009). https://doi.org/10.1523/JNEUROSCI.0764-09.2009. Accessed 2019-11-22

[32] Scheffer, L.K., Xu, C.S., Januszewski, M., Lu, Z., Takemura, S.-y., Hayworth, K.J., Huang, G.B., Shinomiya, K., Maitlin-Shepard, J., Berg, S., Clements, J., Hubbard, P.M., Katz, W.T., Umayam, L., Zhao, T., Ackerman, D., Blakely, T., Bogovic, J., Dolafi, T., Kainmueller, D., Kawase, T., Khairy, K.A., Leavitt, L., Li, P.H., Lindsey, L., Neubarth, N., Olbris, D.J., Otsuna, H., Trautman, E.T., Ito, M., Bates, A.S., Goldammer, J., Wolff, T., Svirskas, R., Schlegel, P., Neace, E., Knecht, C.J., Alvarado, C.X., Bailey, D.A., Ballinger, S., Borycz, J.A., Canino, B.S., Cheatham, N., Cook, M., Dreher, M., Duclos, O., Eubanks, B., Fairbanks, K., Finley, S., Forknall, N., Francis, A., Hopkins, G.P., Joyce, E.M., Kim, S., Kirk, N.A., Kovalyak, J., Lauchie, S.A., Lohff, A., Maldonado, C., Manley, E.A., McLin, S., Mooney, C., Ndama, M., Ogundeyi, O., Okeoma, N., Ordish, C., Padilla, N., Patrick, C.M., Paterson, T., Phillips, E.E., Phillips, E.M., Rampally, N., Ribeiro, C., Robertson, M.K., Rymer, J.T., Ryan, S.M., Sammons, M., Scott, A.K., Scott, A.L., Shinomiya, A., Smith, C., Smith, K., Smith, N.L., Sobeski, M.A., Suleiman, A., Swift, J., Takemura, S., Talebi, I., Tarnogorska, D., Tenshaw, E., Tokhi, T., Walsh, J.J., Yang, T., Horne, J.A., Li, F., Parekh, R., Rivlin, P.K., Jayaraman, V., Costa, M., Jefferis, G.S., Ito, K., Saalfeld, S., George, R., Meinertzhagen, I.A., Rubin, G.M., Hess, H.F., Jain, V., Plaza, S.M.: A connectome and analysis of the adult Drosophila central brain. eLife **9**, 57443 (2020). https://doi.org/10.7554/eLife.57443. Accessed 2021-09-01

[33] Takemura, S.-y., Aso, Y., Hige, T., Wong, A., Lu, Z., Xu, C.S., Rivlin, P.K., Hess, H., Zhao, T., Parag, T., Berg, S., Huang, G., Katz, W., Olbris, D.J., Plaza, S., Umayam, L., Aniceto, R., Chang, L.-A., Lauchie, S., Ogundeyi, O., Ordish, C., Shinomiya, A., Sigmund, C., Takemura, S., Tran, J., Turner, G.C., Rubin, G.M., Scheffer, L.K.: A connectome of a learning and memory center in the adult Drosophila brain. eLife **6**, 26975 (2017). https://doi.org/10.7554/eLife.26975. Accessed 2019-11-22

[34] Sakmann, B.: Single-Channel Recording, 2. ed edn. Springer, New York [u.a] (2009)

[35] Hige, T., Aso, Y., Modi, M.N., Rubin, G.M., Turner, G.C.: Heterosynaptic Plasticity Underlies Aversive Olfactory Learning in Drosophila. Neuron **88**(5), 985–998 (2015)

[36] Zheng, Z., Lauritzen, J.S., Perlman, E., Robinson, C.G., Nichols, M.,

Milkie, D., Torrens, O., Price, J., Fisher, C.B., Sharifi, N., Calle-Schuler, S.A., Kmecova, L., Ali, I.J., Karsh, B., Trautman, E.T., Bogovic, J.A., Hanslovsky, P., Jefferis, G.S.X.E., Kazhdan, M., Khairy, K., Saalfeld, S., Fetter, R.D., Bock, D.D.: A Complete Electron Microscopy Volume of the Brain of Adult Drosophila melanogaster. Cell **174**(3), 730–74322 (2018)

[37] Hines, M.L., Carnevale, N.T.: The Neuron Simulation Environment. Neural Computation **9**(6) (1997)

[38] Niebur, E.: Neuronal Cable Theory. Scholarpedia **3**(5), 2674 (2008)

[39] Barnstedt, O., Owald, D., Felsenberg, J., Brain, R., Moszynski, J.-P., Talbot, C.B., Perrat, P.N., Waddell, S.: Memory-Relevant Mushroom Body Output Synapses Are Cholinergic. Neuron **89**(6), 1237–1247 (2016). https://doi.org/10.1016/j.neuron.2016.02.015. Accessed 2019-11-22

[40] Su, H., O'Dowd, D.K.: Fast synaptic currents in Drosophila mushroom body Kenyon cells are mediated by α-bungarotoxin-sensitive nicotinic acetylcholine receptors and picrotoxin-sensitive GABA receptors. Journal of Neuroscience **23**(27), 9246–9253 (2003)

[41] Hige, T., Aso, Y., Rubin, G.M., Turner, G.C.: Plasticity-driven individualization of olfactory coding in mushroom body output neurons. Nature **526**(7572), 258–262 (2015). https://doi.org/10.1038/nature15396

[42] Owald, D., Waddell, S.: Olfactory learning skews mushroom body output pathways to steer behavioral choice in Drosophila. Current Opinion in Neurobiology **35**, 178–184 (2015). https://doi.org/10.1016/j.conb.2015.10.002. Accessed 2019-11-22

[43] Pai, T.-P., Chen, C.-C., Lin, H.-H., Chin, A.-L., Lai, J.S.-Y., Lee, P.-T., Tully, T., Chiang, A.-S.: Drosophila ORB protein in two mushroom body output neurons is necessary for long-term memory formation. Proceedings of the National Academy of Sciences **110**(19), 7898–7903 (2013). https://doi.org/10.1073/pnas.1216336110. Accessed 2021-01-27

[44] Delestro, F., Scheunemann, L., Pedrazzani, M., Tchenio, P., Preat, T., Genovesio, A.: In vivo large-scale analysis of Drosophila neuronal calcium traces by automated tracking of single somata. Scientific Reports **10**(1), 7153 (2020). https://doi.org/10.1038/s41598-020-64060-x. Accessed 2020-06-13

[45] Shyu, W.-H., Lee, W.-P., Chiang, M.-H., Chang, C.-C., Fu, T.-F., Chiang, H.-C., Wu, T., Wu, C.-L.: Electrical synapses between mushroom body neurons are critical for consolidated memory retrieval in Drosophila. PLOS Genetics **15**(5), 1008153 (2019). https://doi.org/10.1371/journal.pgen.1008153. Accessed 2019-11-22

[46] Warth Pérez Arias, C.C., Frosch, P., Fiala, A., Riemensperger, T.D.: Stochastic and Arbitrarily Generated Input Patterns to the Mushroom Bodies Can Serve as Conditioned Stimuli in Drosophila. Frontiers in Physiology **11**, 53 (2020). https://doi.org/10.3389/fphys.2020.00053. Accessed 2020-03-03

[47] Li, F., Lindsey, J.W., Marin, E.C., Otto, N., Dreher, M., Dempsey, G., Stark, I., Bates, A.S., Pleijzier, M.W., Schlegel, P., Nern, A., Takemura, S.-y., Eckstein, N., Yang, T., Francis, A., Braun, A., Parekh, R., Costa, M., Scheffer, L.K., Aso, Y., Jefferis, G.S., Abbott, L.F., Litwin-Kumar, A., Waddell, S., Rubin, G.M.: The connectome of the adult Drosophila mushroom body provides insights into function. eLife **9**, 62576 (2020). https://doi.org/10.7554/eLife.62576. Accessed 2021-03-09

[48] Berry, J.A., Phan, A., Davis, R.L.: Dopamine Neurons Mediate Learning and Forgetting through Bidirectional Modulation of a Memory Trace. Cell Reports **25**(3), 651–6625 (2018). https://doi.org/10.1016/j.celrep.2018.09.051. Accessed 2019-11-22

[49] Yamagata, N., Ichinose, T., Aso, Y., Plaçais, P.-Y., Friedrich, A.B., Sima, R.J., Preat, T., Rubin, G.M., Tanimoto, H.: Distinct dopamine neurons mediate reward signals for short- and long-term memories. Proceedings of the National Academy of Sciences **112**(2), 578–583 (2015). https://doi.org/10.1073/pnas.1421930112. Accessed 2020-03-03

[50] Burke, C.J., Huetteroth, W., Owald, D., Perisse, E., Krashes, M.J., Das, G., Gohl, D., Silies, M., Certel, S., Waddell, S.: Layered reward signalling through octopamine and dopamine in Drosophila. Nature **492**(7429), 433–437 (2012). https://doi.org/10.1038/nature11614. Accessed 2019-11-22

[51] Bouzaiane, E., Trannoy, S., Scheunemann, L., Plaçais, P.-Y., Preat, T.: Two Independent Mushroom Body Output Circuits Retrieve the Six Discrete Components of Drosophila Aversive Memory. Cell Reports **11**(8), 1280–1292 (2015). https://doi.org/10.1016/j.celrep.2015.04.044. Accessed 2019-11-22

[52] Cassenaer, S., Laurent, G.: Hebbian stdp in mushroom bodies facilitates the synchronous flow of olfactory information in locusts. Nature **448**(7154), 709 (2007)

[53] Rumsey, C.C., Abbott, L.F.: Synaptic democracy in active dendrites. Journal of Neurophysiology **96**(5), 2307–2318 (2006)

[54] Sterratt, D.C., Groen, M.R., Meredith, R.M., Van Ooyen, A.: Spine calcium transients induced by synaptically-evoked action potentials can predict synapse location and establish synaptic democracy. PLoS Comput Biol **8**(6), 1002545 (2012)

[55] Froemke, R.C., Poo, M.-m., Dan, Y.: Spike-timing-dependent synaptic plasticity depends on dendritic location. Nature **434**(7030), 221–225 (2005)

[56] Gidon, A., Segev, I.: Spike-timing–dependent synaptic plasticity and synaptic democracy in dendrites. Journal of neurophysiology **101**(6), 3226–3234 (2009)

[57] Ravenscroft, T.A., Janssens, J., Lee, P.-T., Tepe, B., Marcogliese, P.C., Makhzami, S., Holmes, T.C., Aerts, S., Bellen, H.J.: Drosophila voltage-gated sodium channels are only expressed in active neurons and are localized to distal axonal initial segment-like domains. Journal of Neuroscience **40**(42), 7999–8024 (2020)

[58] Abdelrahman, N.Y., Vasilaki, E., Lin, A.C.: Compensatory variability in network parameters enhances memory performance in the *drosophila* mushroom body. Proc. Nat. Acad. Sci., USA **118**(49) (2021). e2102158118

[59] Baltruschat, L., Prisco, L., Ranft, P., Lauritzen, J.S., Fiala, A., Bock, D.D., Tavosanis, G.: Circuit reorganization in the Drosophila mushroom body calyx accompanies memory consolidation. Cell Reports **34**(11), 108871 (2021). https://doi.org/10.1016/j.celrep.2021.108871. Accessed 2021-03-24

[60] Pfeiffer, B.D., Ngo, T.-T.B., Hibbard, K.L., Murphy, C., Jenett, A., Truman, J.W., Rubin, G.M.: Refinement of Tools for Targeted Gene Expression in Drosophila. Genetics **186**(2), 735–755 (2010). https://doi.org/10.1534/genetics.110.119917. Accessed 2019-11-22

[61] Schindelin, J., Arganda-Carreras, I., Frise, E., Kaynig, V., Longair, M., Pietzsch, T., Preibisch, S., Rueden, C., Saalfeld, S., Schmid, B., Tinevez, J.-Y., White, D.J., Hartenstein, V., Eliceiri, K., Tomancak, P., Cardona, A.: Fiji: An open-source platform for biological-image analysis. Nature Methods **9**(7), 676–682 (2012). https://doi.org/10.1038/nmeth.2019. Accessed 2020-03-03

[62] Wilson, R.I.: Transformation of Olfactory Representations in the Drosophila Antennal Lobe. Science **303**(5656), 366–370 (2004). https://doi.org/10.1126/science.1090782. Accessed 2020-03-03